



Radio Frequency Magnetron Sputtering Coatings of Biomedical Implants Using Nanostructured Titanium Carbide Thin films

Akinsanya D. Baruwa¹ · Olayinka O. Abegunde² · Esther T. Akinlabi³ · Oluseyi P. Oladijo^{1,4} · Elizabeth M. Makhatha¹ · Omolayo M. Ikumapayi⁵ · Shree Krishna⁶ · Jyotsna Dutta Majumdar⁷

Received: 5 July 2021 / Revised: 17 August 2021 / Accepted: 23 August 2021 / Published online: 30 August 2021
© The Author(s), under exclusive licence to Springer Nature Switzerland AG 2021

Abstract

RF Magnetron sputtering is a distinctive deposition process that has applicability for growing thin film coatings on the surface of any materials such as biomedical implants without the formation of excessive heat and alteration of the overall properties of the materials. In this research study, a 99.5% purity nanostructured titanium carbide (TiC) target was effectively deposited on biomedical implants (Ti6Al4V) substrates under various sputtering process parameters. A field emission scanning electron microscope was used to analyse the surface morphology, and an atomic force microscope was used to probe the topography of the thin film coatings. Low angle X-ray diffractometer and Raman spectroscopy were used to investigate the phase formation and structural properties of the thin film coatings to consolidate the surface characterisation. The young modulus and hardness of the TiC thin film coatings were investigated using nanoindentation. The evolving microstructure and surface roughness show significant reliance on the process parameters. All the thin film coatings are oriented towards (200) planar. From the grain sizes calculations, it was observed that samples produced at higher process parameters (RF power and temperature) exhibit the most diminutive grain sizes. All samples prepared at higher process parameters show an improved mechanical strength. It also established that sample L4 prepared at the highest temperature and higher RF power displayed the most robust properties.

Keywords RF magnetron sputtering · Process parameters · Thin film coating · Titanium · Titanium carbide

1 Introduction

Titanium is regarded as a low-density metal by having nearly 50% of the density of cobalt and 60% of the density of steel and iron. Titanium and its alloys have been grouped into four different categories depending on the ratio of the alloying elements, namely α alloys, near- α alloys, α - β alloys, and β alloys [1–3]. Titanium alloy offers unique properties, including low elastic modulus, excellent corrosion and wear-resistant, and superior mechanical properties [3]. Due to all these significant properties, titanium and its alloys have been substantiated as one of the leading and most adaptable materials used for several applications, and it is fast becoming the material of choice for implants and dental applications [4]. Stainless steel and cobalt alloys have also been used for biomedical implants but tend to react with the body fluid, which usually leads to corrosion of the material, resulting in damage to the tissues [5]. The main feature that distinguished titanium and its alloys from other materials is its biocompatibility.

✉ Olayinka O. Abegunde
abegunde.oluwatosin@um6p.ma

- ¹ Metallurgical Engineering, University of Johannesburg, Johannesburg 2028, South Africa
- ² Department of Materials Science, Energy and Nano-Engineering, Mohammed VI Polytechnic University, BenGuerir, Morocco
- ³ Pan African University of Life and Earth Science, Ibadan, Nigeria
- ⁴ Department of Chemical, Materials and Metallurgical Engineering, Botswana International University of Science and Technology, Private Bag 16, Palapye, Botswana
- ⁵ Department of Mechanical and Mechatronics Engineering, Afe Babalola University, Ado Ekiti, Nigeria
- ⁶ School of Nanoscience & Technology, Indian Institute of Technology, Kharagpur 721302, West Bengal, India
- ⁷ Department of Metallurgy and Materials Engineering, Indian Institute of Technology, Kharagpur 721302, West Bengal, India

It has a broad spectrum of biomedical applications, which include its good corrosion resistance, a low ion-formation and release of toxic elements in aqueous environments, resistance to body fluids, the quick stable and inert layer surface film formation, good adaptability to the tissues, non-biodegradation or decomposition in body and its biocompatibility [6, 7]. Also, titanium has superior mechanical properties such as high tensile strength, good compressibility, adequate ductility, high elongation, sufficient fatigue strength, as well as bending and shearing abilities [8]. Another industry in which titanium has been widely utilised and exploited is aerospace and aviation due to its high strength-to-weight ratio, favourable working temperature, composite compatibility with polymers, good damage tolerance, mechanical properties, and excellent corrosion resistance [9, 10]. The focal point usage of titanium in the aerospace industry is tubes, the fan turbine blade, missile fins, and advanced aircraft and spacecraft airframes [11, 12]. Other prominent industrial applications of titanium alloys are the automobile industry [13], the marine industry [14] and space applications [15].

Although titanium possesses good mechanical properties and corrosion resistance, titanium and its alloys exhibit weaknesses and limitations such as the stress shielding phenomenon, biomechanical compatibility, reduced bio-functional application or osseointegration, and inferior tribology and low abrasion resistance [16–18]. Titanium alloys are considered reactive materials and often generate a protective layer spontaneously when exposed to ambient atmospheric conditions. This inhibits the propagation of corrosion in the presence of oxygen. However, it loses its ability to regenerate the protective oxide film in an anhydrous condition, resulting in corrosion. With all these limitations, it is important to protect the surface properties of titanium alloys, with none or a minimal change to the overall bulk properties of the material. Coating the surface with nanoscale or nanostructured materials in the form of a thin or thick film is a potential way of mitigating these shortcomings. Nanostructured thin film coatings have been investigated and reported to increase the material's performance, improving mechanical and surface properties. Consequently, they enhance the yield of the surface reactions of interest [15].

Nowadays, titanium carbide coatings are attractive for the technological and scientific communities owing to their excellent properties, such as extreme thermal stability, high melting point (3067 °C), superior surface hardness (26–30 GPa), which is greater than the typical microhardness of ZrN (16 GPa), TiN (20 GPa), and ZrC (23 GPa). Other properties include high electrical conductivity, oxidation resistance, excellent chemical stability, elastic moduli, resistance to creep/thermal shock, low reactivities, good corrosion resistance, low wear rate and the low friction coefficient of TiC [19–23]. These extraordinary properties exhibited by

TiC are associated with its high energy of cohesion and its chemical bonding.

Diverse techniques have been established to grow thin film on the surface and curb these demerit factors, limiting the potential failure of titanium and its alloys [24]. In this present study, TiC was sputtered on Ti6Al4V titanium alloys at the nanoscale level using RF magnetron sputtering. Depositing titanium carbide at the nanoscale on different materials using RF Magnetron sputtering has not been widely investigated. Different characterisation methods were used to investigate and analyse the TiC thin film coatings to determine a suitable window sputtering parameter for the coating process.

2 Deposition and Characterisation Process

2.1 Thin Film Coating Process

RF magnetron sputtering machine was used to deposit TiC thin films on Ti6Al4V (90.0 Ti, 0.05 V, 0.08 C, 0.015 H, 0.40 Fe, 0.20 O, 5.50–6.75 Al, 3.50–4.50 V wt. %) substrates at staggered radio frequency power, substrate heating temperature and the process sputtering time. The Ti6Al4V substrates were prepared using waterproof silicon carbide papers of grits 120, 480, 600 and 1200, and afterwards polished to have an ultra-smooth surface. Furthermore, contaminants were removed from the surface by rinsing the substrates with acetone and ethanol prior to deposition of TiC thin film coatings. The TiC target used was of 99.5% purity and supplied by HHV, United Kingdom. During the process, the optimised process parameters were reached by varying sputtering power, time and temperature while keeping other parameters such as the argon gas flow rate, base pressure, working pressure and substrate-target distance were kept constant. The RF Magnetron sputter was operated at 13.56 Hz. To further remove the surface impurities and target contaminants, pre-sputtering was implemented on every sample for 15 min. The average thickness of the TiC coatings measured using Calotest was found to be $1 \mu\text{m} \pm 20 \text{ nm}$. The flow chart of the experimental details can be found in Fig. 1. The experimental matrix is presented in Table 1, and the deposition sequence for acceptable coatings is presented in Fig. 1.

2.2 Experimental Characterisation

Field Emission Scanning Electron Microscope (FESEM) model Gemini*2 made by ZEISS was used to characterise the microstructural evolutions of the thin film coatings with a magnification of 50,000 \times . The surface topography and roughness were investigated using Veeco Di2100 atomic force microscope AFM. The AFM was performed in tapping

Fig. 1 Experimental flow chart

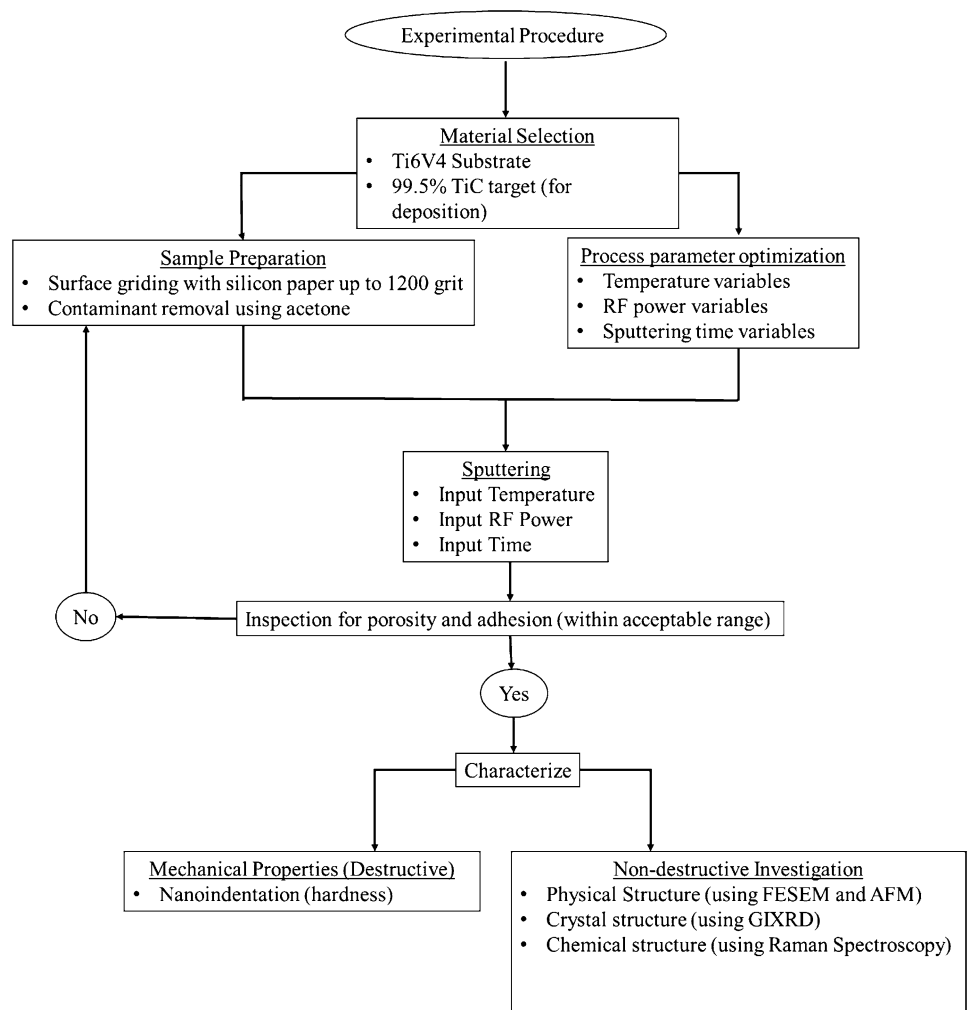


Table 1 Experimental process matrix of RF magnetron sputtering

Process parameters	RF power (W)	Temperature (°C)	Sputtering time (Hrs)
L1	150	80	2
L2	150	90	2.5
L3	150	100	3
L4	200	100	2
L5	200	80	2.5
L6	200	90	3
L7	250	100	2
L8	250	80	2.5
L9	250	90	3

working mode at the ambient condition to eliminate compromising the surface artefacts. The scanning and capturing of the surfaces were done of $5 \times 5 \mu\text{m}^2$. The x-ray characterisation of the thin film coatings was performed on PANalyticals's Xpert Pro with Cu $K\alpha$ radiation, scanning incidence of $0.02^\circ/\text{s}$ from 10° to 90° , and wavelength 1.540598

A Grazing Incidence X-ray Diffractometer GIXRD. The Scherer equation [25] was used to determine the grain size of the coating. The Scherer equation is presented in Eq. (1).

$$D = \beta \cos \theta \frac{0.9\lambda}{\beta \cos \theta} \tag{1}$$

The microstrain, dislocation density and texture coefficient were also calculated from the GIXRD results. The equations used are presented in Eqs. (2), (3) and (4), respectively.

$$\text{Microstrain} = \frac{\beta \cos \theta}{4} \tag{2}$$

$$\text{Dislocation density} = \frac{1}{D^2} \tag{3}$$

$$\text{Texture coefficient} = \frac{I_{(hkl)}/I_{0(hkl)}}{\sum_N I_{hkl}/I_{0(hkl)}} \times 100\% \tag{4}$$

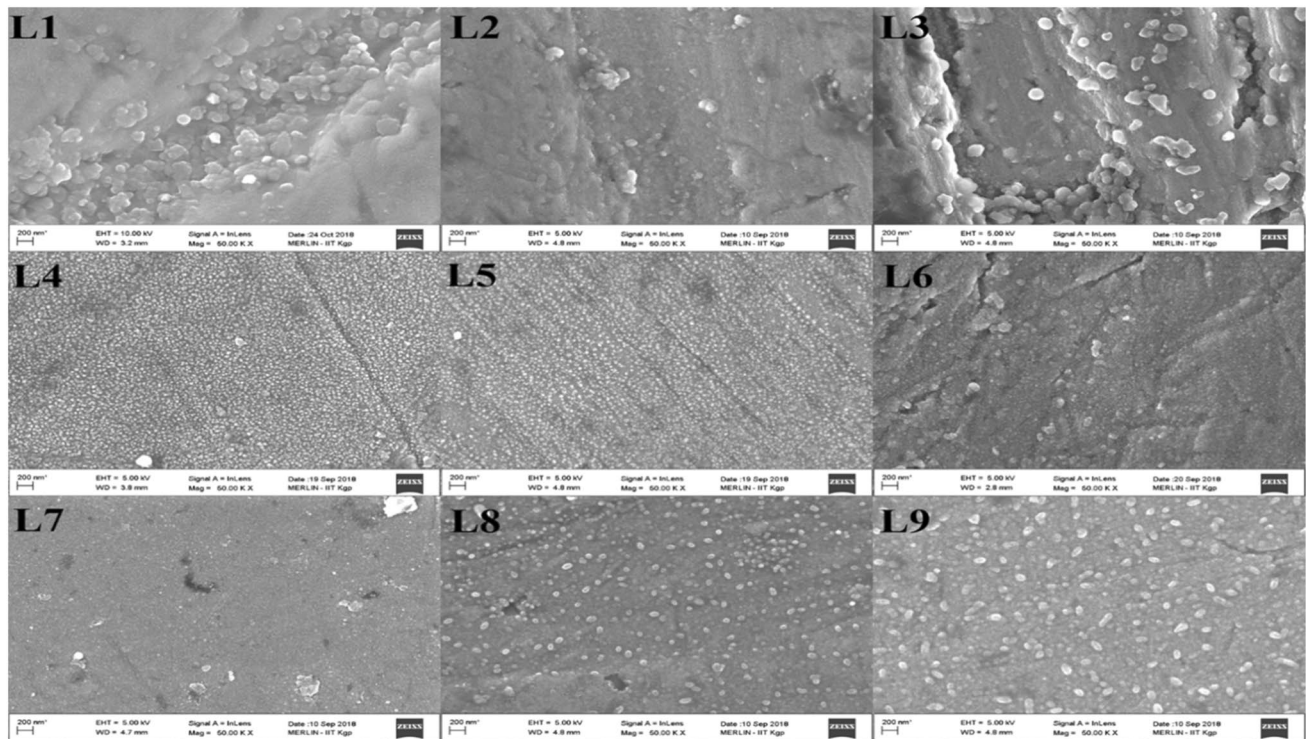


Fig. 2 Planar view of the surface morphology of Ti6Al4V/TiC thin film coatings

where β is the full width at half maximum intensity (FWHM), θ is the Bragg's angle, λ represents the wavelength of the X-ray equipment, D is the crystalline grain size, N is the number of reflections in the XRD, $I_{(hkl)}$ is the measured intensity of the plane from the TiC spectra and $I_{0(hkl)}$ is the integral intensity of the TiC sample with complete randomly oriented (hkl) plane taken from the ICDD-JCPDS Cards (titanium carbide no. 32-1383).

Alpha300R Raman spectroscopy microscope (WITec) equipped with a frequency-doubled Nd-YAG laser of wavelength 532 nm was used to measure the Raman spectroscopy of the TiC thin film coatings. The Raman spectra were obtained at a magnification of 50 \times on Nikon objectives lenses. To avert the burning or damage of the thin film coatings, a lower laser power of 2 mW was adopted, and all the analyses were conducted at room temperature in order. Before the acquisition of spectra, calibration and beam centring was performed with a-Si standard (111). For comparison and analysis, the spectrum of the substrate was also measured.

Hysitron, Triboindenter TI950 nanoindentation was used to determine the films' mechanical properties (hardness and Young modulus). The measurements were taken using load-controlled mode. The holding time was 15 s at the peak load before unloading the indenter. The peak load was 5 N. Berkovich diamond indenter with a tip radius of curvature of 100 nm was used. The young modulus of the TiC thin films

was extrapolated from the measured load against displacement curves using the Oliver and Pharr method [26, 27]. An average of 16 measurements was taken at different locations on the thin film coating for each sample. The indentation depth was restricted to 10% of the coating thickness for all the samples to eliminate the impact of the substrate on the thin film coating [28].

3 Experimental Result

3.1 Physical Structure Analysis

The microstructural evolutions of the planar view acquired from the FESEM are presented in Fig. 2. The FESEM morphology images were taken at a magnification of 50000 \times . It was observed that the samples produced at the same RF power portray similar morphology and geometry features. This indicates that the RF power substantially affects the nucleation and the growth of TiC thin films. However, the impact of the sputtering time and the substrate temperature were also taken into consideration. Since RF magnetron sputtering coating is a non-equilibrium process, having a universal growth mechanism to describe all the coating becomes impossible. Consequently, the microstructural evolution behaviours under different process parameters differ in their morphology. TiC thin films were formed on

the substrates by condensing the TiC adatoms and growth nucleation. The deposition, nucleation and growth mechanism of the coatings rely on the bonding interaction between the substrate surface and the condensing target adatoms. The substrate temperature, the RF power and the sputtering time also influence the surface mobility of the coatings. Three distinct morphological zones are noticeable for all the samples, and these correspond to different growth zones. The first morphological zone is noticeable with samples produced at 150 W (which are samples L1, L2 and L3, respectively). The growth mechanism is similar to that of the Van der Merwe pattern or the Island growth mechanism. This type of growth model is characterised by the presence of rough and porous surface morphology and crystallographic mismatch due to inadequate surface diffusion of the condensing TiC adatoms [24]. The films contain cracks and voids which grow with an increase in the temperature for samples L1, L2 and L3. It is assumed that the deposition rate of the condensing TiC adatoms on the substrate surface is faster than the surface diffusion and nucleation rate. The slow rate of surface diffusion causes the clusterisation of atoms at the early stages of the thin film growth and leads to a wide range of discrete sizes, followed by the side-wall growth of clusters caused by the shadowing effect. For samples produced at 200 W (which are samples L4, L5 and L6, respectively), high-quality uniform and continuous coverage of TiC thin film on the substrate, with a very flat surface, and meagre cracks were noticed for both coatings. Chemisorption was dominant in the growing process with a strong bond between the TiC adatoms and Titanium grade 5 substrates. This denotes good or strong adhesion between the substrates and the thin films. The TiC thin films show asymmetrical nanostructured geometry due to the coalescence of the individual islands, leading to continuous undisturbed columnar growth [29]. The TiC nuclei primarily grow on the substrate by Volmer Weber or by a layer to layer growth mechanism. This growth type arises when film atoms bond together rather than the substrate, with a minimal breakaway from the coating [29]. This zone is characterised by dense equiaxed coatings and uniform surfaces due to the properly controlled surface diffusion growth mechanism of the TiC adatoms. The nucleation size of the adatoms generally increases with increasing substrate temperature for samples L4, L5 and L6, respectively. As the deposition power increased to 200 W, the dynamic of the surface growth also changes from a shadowing effect to a re-emission process. Non-sticking TiC atoms are re-emitted while they reach other points on the surface with a shadowed valley included. The resputtering effect, which involved knocking off a surface atom and the redeposition thereof in a valley of the substrate, also occurred. The re-emission and the re-sputtering process have a smoothening effect on the TiC thin film coating at an RF power of 200 W. The emerging of a new growth mode associated with 200 W

RF power could be ascribed to the enhancement and increase surface energy and the energy of the incident adatoms. An increase in RF power results in higher surface mobility of the adatoms, improves surface diffusion of the adatoms, reduces the shadowing effect around the growth region, and reduces the porosity fraction [29, 30]. The atomic mobility of the thin films is improved as a result of high incident energy ion bombardment. It thereby promotes the condensation of the adatoms condensation, high densification of the TiC adatoms. This occurs at the surface concavities, which leads to a smoother surface and more densely packed TiC thin films coating. Further nucleation and different growth patterns were seen at an RF power of 250 W, samples L7, L8 and L9, respectively. Two types of TiC thin films crystal morphology co-exist within the coating layers. This type of coating morphology was also reported by Baric et al. [31] in their work. The samples show high film densification, with an equiaxed structure at the bottom and a large scanty partially destructed columnar structure at the top, compared with an evenly distributed coating observed at the RF power of 200 W. This means that both parallel and perpendicular modes were dominant in the formation of the TiC thin film coating on the substrates. The parallel mode was caused by the surface diffusion of the adatom, which might be responsible for the equiaxed grain seen at the bottom [29]. The perpendicular mode involves the impingement of the incident TiC adatoms, causing the perpendicular growth of another layer, and the probability of new clusters formation arises [29]. This phenomenon is analogous to the Stranski-Krastanov (S-K) growth mechanism [32]. The shadowing and re-emission effects show to be the dominant growth pattern for the TiC thin film at 250 W power. The irregular grain shape and the orientation noticed at 250 W could also be attributed to agglomeration and the coalescence of new atoms. The effect could have been caused by the atomic peening effect. The heterogeneous nature of the process parameters leads to the larger size of the sputtered particles and the formation of new layers.

The AFM surface topography provides more information on the surface roughness at the nanoscale level. The 3D surface topography of the height images TiC thin film coatings are represented in Fig. 3. The AFM artefacts of the thin film coatings exhibit columnar surface topography. These columnar structures developed in two directions, namely the lateral and vertical direction as seen in the Figures. The formation of the columnar structure observed is in agreement with the microstructural evolution observation. From AFM images, the concentration of the Titanium carbide nanoparticle coatings increases as the deposition power, temperature and sputtering time increase. Samples L1, L2, and L3, produced at 150 W, show high dominance of both peaks and valleys in the surface topography. From observations, once the power increased to 200 W in samples L4, L5 and L6, the TiC

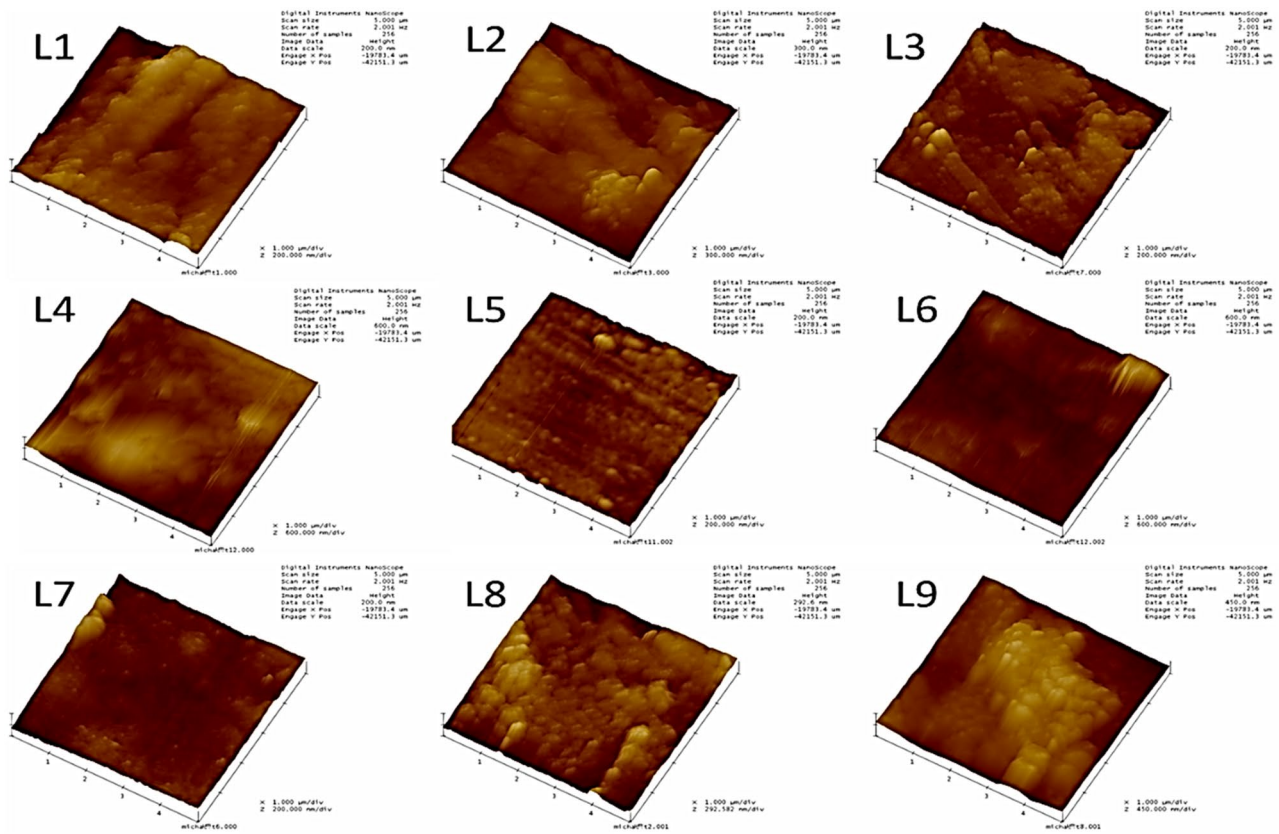


Fig. 3 AFM 3D height surface topography of Ti6Al4V/TiC thin film coatings

coatings covered more surface areas with a reduction in the concentration of valleys and increment of the peak regions. The decrease in the valley could be attributed to the resputtering effect caused by the high energy of the impinging adatoms. As the process parameters increase, more adatoms are ejected from the TiC targets. These adatoms strike the condensed atoms on the surface of the substrates, thereby causing the redistribution and re-condensation of the atoms

lower valleys or regions on the substrates. At 250 W, most of the valleys observed at lower power have been filled up with TiC nanoparticles coating. The reduction in the valleys and better surface area distribution of the TiC coatings with an increase in power can be attributed to the faster ejection of TiC atoms from the targets and increase in the rate of condensation of the adatoms on the substrates. The surface diffusion of the TiC nanoparticles increases with power, leading to an increase in growth rate and TiC concentration on the surface. Chawla et al. [33] reported that the adatom mobility and deposition rate increase with RF power. Such phenomenon results in the growth of finer crystallite size with homogenous distribution of the thin films. In addition, the TiC films agglomeration become thicker and denser with an increase in deposition time. An increase in time has been reported to improve grain growth, reduce surface roughness, and increase the film coatings' density [34]. Clustering and roughening were also noticed in the films with each increase in temperature in all the coatings.

Table 2 AFM statistical results for Ti6Al4V/TiC thin film coatings

S/N	Mean roughness (nm)	RMS (nm)	Maximum height (nm)	Surface skewness	Coefficient of kurtosis
L1	28.13	36.69	231.78	0.109	3.525
L2	35.65	44.99	335.69	0.101	3.202
L3	20.72	26.45	207.18	0.193	3.684
L4	12.496	14.31	176.24	0.358	2.660
L5	11.68	14.66	132.70	0.131	3.394
L6	12.34	15.96	186.33	1.387	3.154
L7	17.19	23.72	203.08	1.740	3.857
L8	25.39	32.62	199.46	0.177	3.070
L9	20.80	27.05	171.17	0.170	3.261

The statistical surface topography result of the thin film coatings, such as surface roughness (mean and RMS), maximum height, surface skewness and coefficient of Kurtosis are collected and presented in Table 2. The surface roughness for Ti6Al4V/TiC thin film ranges from 11 to 60 nm.

The high roughness value at samples produced at 150 W was due to the formation of deep channels and the island growth morphology on the film surface. However, from the surface topography in this study, it is also established that the surface roughness reduces with an increase in the process parameters. The increase in process parameters results in smoother film surfaces and a reduction in surface roughness. The least roughness on the surfaces considered was found at a range of samples produced at 200 W (samples L4, L5 and L6). Samples produced at 200 W have uniform surface distribution and smoother surface, contributing to the surface roughness behaviour. The asymmetry and flatness profiling of the samples were also analysed using the surface skewness, which measures the profile symmetry about the mean line and the kurtosis coefficient of the film coatings, which measures the surface sharpness of the film coatings.

To have a perfectly symmetrical height profile, the surface skewness should be zero. However, suppose the height profile distribution of the surface is asymmetrical and characterised with more peaks than valleys. In that case, the Skewness moment is positive, and if the surface valleys are predominant with minimal peaks, the Skewness is negative. From the AFM statistical analysis, the values obtained for all the coating are positive. This denotes that the coatings contain more peaks of TiC thin films than the valley. There are terms associated with the roughness of surfaces. The term Mesokurtic is referred to a Gaussian amplitude distribution when the Kurtosis coefficient is 3. It is referred to as Plat-

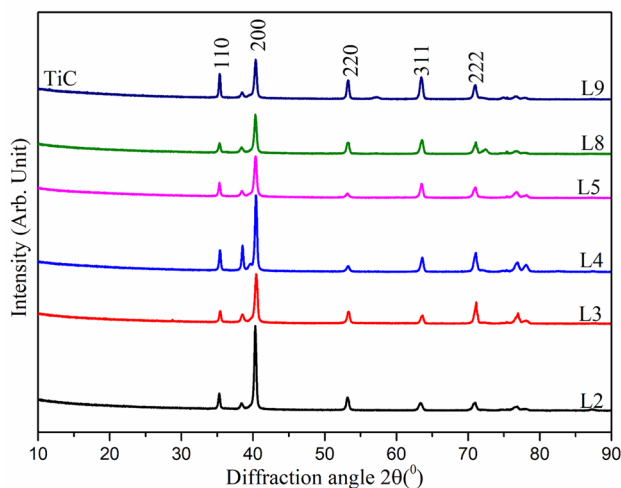


Fig. 4 GIXRD spectra of Ti6Al4V/TiC coatings

ykurtic when the distribution shows a Kurtosis value of less than 3. If the Kurtosis exceeds 3, it is called leptokurtic, and the surface has more peaks than valleys. The predominant mode for all the coatings is leptokurtic, suggesting that the

surface of the TiC thin films are concentrated with extreme peaks of TiC thin films distribution.

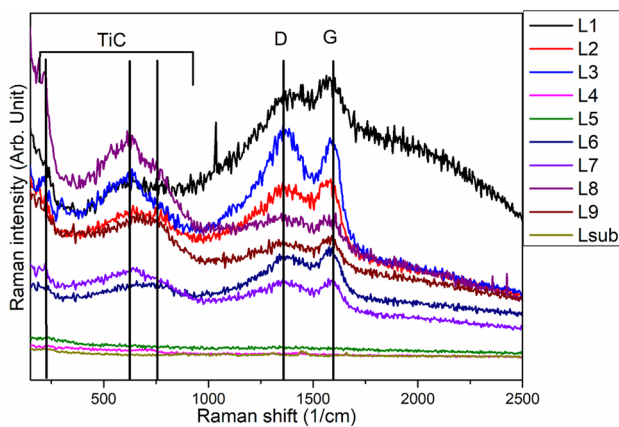
3.2 Crystallinity Analysis

GIXRD analysis of selected samples is presented in Fig. 4. The (200) orientation plane is found to be the main preferential orientation peak in all the coatings. Other noticeable orientation peaks from the GIXRD analysis are (110), (220), (311) and (222) diffraction peaks. All these peaks are associated with TiC thin film. This validates the purity and stability of the TiC target during deposition. To further quantify the crystalline quality of the films, some parameters, including the diffraction angle (2θ), d-spacing, full width at half maximum (FWHM), crystalline size, dislocation density, microstrain and texture coefficient of the TiC thin film produced using different process parameters were analysed and presented in Table 3. The texture coefficients (TC) of all the main diffraction peaks were calculated. The texture coefficient is calculated using the equation of the Harris formula [35, 36]. For a standard sample, the texture coefficient is one for all the (hkl) orientation planes. The maximum texture coefficient was found in the (200) plane, showing the appreciably high preferential orientation of the TiC film. The value of the TC indicates the surface of the coatings with the most effective peaks in the GIXRD analysis. The calculated grain sizes of the TiC thin film crystallite using the Debye–Scherrer are also presented in Table 3. The least grain size range was found at samples produced at 200 W. Resputtering of the TiC adatoms can occur on the thin film if the process parameters are increased, and this could cause the formation of TiC grains of different sizes and geometry.

The possible reasons could be the penetration of encroaching ions into the lattice structure of the condensed film and the reduction in the generation of pores and defects. This action would lead to an increasing count of preferential nucleation sites, which could result in smaller grains [37]. The microstrain and the dislocation density of the TiC thin films were also calculated. The microstrain is a manifestation of the dislocation network and the stress in the films by producing a local strain close to the defect. The dislocation density has been described as the number of dislocation lines per unit volume. The outcome of the dislocation density shows the different degrees of variance in the behavioural pattern of the TiC coating. The outcome tends to reduce for most of the coating as the deposition parameters increase, which indicates a reduction in the lattice deficiency, and it exhibits good crystallinity. The d-spacing obtained from the GIXRD investigation was compared with the standard ASTM d-spacing of titanium carbide. Comparing the TiC thin films d-spacing with the standard ASTM structure shows that the d-spacing of the (200) preferential orientation

Table 3 GIXRD data for TiC coatings on Ti6Al4V

Experi-mental run	2 θ (°)	d spacing (Å)	D ASTM (Å)	FWHM (°)	(hkl)	Crystalline size (nm)	Dislocation density (δ) (Lines/m ²) $\times 10^{14}$	Micro strain (ϵ) $\times 10^{-4}$	Texture coefficient
L2	40.4199	2.22977	2.1637	0.0624	200	135.66	0.5433	2.5551	8.72
L3	40.2929	2.23650	2.1637	0.1872	200	45.20	4.8940	7.6684	8.16
L4	40.3925	2.2312	2.1637	0.0936	200	90.44	12.2271	3.8330	6.08
L5	40.3604	2.2329	2.1637	0.078	200	108.51	0.8493	3.1945	5.61
L8	40.3243	2.2367	2.1637	0.1663	200	50.89	3.8614	6.8116	6.14
L9	40.3726	2.2323	2.1637	0.078	200	108.52	0.84922	3.1943	5.35

**Fig. 5** Raman spectroscopy of Ti6Al4V/TiC coatings

plane for all the coatings analysed is above the standard values. A shift to upper values confirms the existence of tensile stress in the thin film coatings.

3.3 Raman Structure

To complement the GIXRD analysis of the TiC thin film crystallinity, Raman spectroscopy analysis was done. The spectra of the coating are presented in Fig. 5. Each spectrum was measured within the range of 100–2500 cm^{-1} with 785 nm excitation light. For each coating, amorphous carbon peaks were visible between the band 1000 and 1900 cm^{-1} . disordered D- band and graphitic G- bands peaks of amorphous carbon were observed at wavelength 1420 and 1530 cm^{-1} . The peaks are due to the presence in the films of sp^2 bonds only [38]. The assignment of the D and G modes are to indicate the molecular structure of carbon defect, and these bonds are present in all the TiC thin film samples, except for the L4 and L5. The D-band is usually responsible for the structural defect and crystalline disorder associated with amorphous carbon in graphites. This coordinates the breathing vibrations of the carbon atoms in the aromatic rings. The G band corresponds to the edge site and the basal

plane of graphite and stretching vibrations of all the sp^2 bonded atoms in both the rings and the chains [39]. The high intensity of the Raman broad bands was visible for those samples prepared at a 150 W RF power. The enhancement of the intensity in these samples may be attributed to the presence of amorphous carbon. Raman vibrations are inactive in stoichiometric TiC compounds due to inverted symmetrical nature [40–42]. These are seen in the Raman spectra of L4 and L5. The lack of high peak intensities in the samples L4 and L5 represent the high crystallinity in the TiC film. However, the formation of TiC/C peaks was detected by the Raman investigation in the remaining samples. Those peaks which correspond to the characteristic features of the TiC compound were found at 245, 610 and 760 cm^{-1} . These are activated by defects like carbon vacancies, which can annihilate the inversion symmetry, and they make some carbon atoms displaced according to Raman active in the crystalline materials [39, 43, 44].

3.4 Mechanical strength

The nanohardness response parameters values were calculated from the load vs displacement relationship, and the values are presented in Table 4. The tables present the values of the hardness (H), Young modulus (E), plasticity index (H/E), wear resistance (H^3/E^2), maximum displacement (H_{max}), final residual indent displacement (H_{res}), % elastic recovery and plasticity. The hardness values increase with the increase in RF power from 150 to 250 W from the analysis of the results. The samples (L1, L2 and L3) produced at 150 W RF power exhibit lower hardness values compare to samples produced at RF power of 200 W (L4, L5 and L6) and 250 W (L7, L8 and L9), respectively. Several reports have established different mechanisms that can improve the mechanical properties of thin film coatings. These mechanisms are interfacial crack deflection, microstructural homogeneity, suppression of dislocation motion, and Hall–Petch strengthening [45–49]. It was noticed that microstructural homogeneity is the predominant mechanism for determining the hardness behaviour of the TiC thin films. The change in the nanohardness properties of the

Table 4 Measured and calculated mechanical properties of Ti6Al4V coated with TiC thin film at different powers

Sample	Hardness H(GPa)	Young modulus E (GPa)	Wear resistance H^3/E^2 (GPa)	Plasticity index H/E	% Elastic recovery	Plasticity
L1	9.17	192.81	0.021	0.048	26.87	73.13
L2	7.80	210.64	0.011	0.037	21.39	78.61
L3	12.89	142.97	0.105	0.090	38.75	61.25
L4	22.27	176.00	0.356	0.127	64.97	35.03
L5	18.26	236.53	0.109	0.077	41.73	58.27
L6	10.49	157.67	0.046	0.067	31.56	68.44
L7	19.37	248.85	0.117	0.078	48.88	51.12
L8	18.61	200.08	0.161	0.093	56.22	43.78
L9	16.26	131.83	0.247	0.123	46.89	53.11

samples is directly related to the microstructural evolution of the samples. Samples produced at 200 W experienced a resputtering effect, resulting in smaller and stable nanostructured grain size, denser film coating and better homogeneity with strong interfaces. This will cause resistance to the mobility of plastic deformation across the boundaries of grains within the matrix. In this kind of condition, a massive amount of mechanical energy would be required to cause plastic deformation, indicating lower penetration depth and improved mechanical properties. Caicedo et al. reported that the existence of grain structures at the nanometer scale in polycrystalline materials causes large-volume fractions of grain boundaries. The grain boundaries initiate dislocation pile-up and hamper dislocation motion. This results in resistance to plastic deformation and improves mechanical properties [50]. The least hardness values were observed in samples L1 and L2, respectively. These samples were prepared at 150 W RF power, and the TiC microstructural evolution were characterised by tunnels and crack. The presence of tunnel and cracks cause weakness in the bonding strength of the thin films, thereby reducing the hardness resistance of the TiC thin films due to lower resistance to deformation and deeper penetration of the indenter. The areas between loading and unloading curves and maximum depth decrease as the nano-hardness increases from the load–displacement plots. There is variance in the Young moduli of coatings even though they are of the same material composition. However, this difference can be attributed to a change in the crystallinity nature of films and phase composition as a result of varied power [51]. Therefore, a reduction in the elastic recovery was visible in the films as a result of an increase in elastic modulus. The reduction will also influence the resistance of the indenter to reach a maximum depth and a resistance to plastic deformation. Other related calculations of the mechanical behaviour were evaluated to get a more in-depth understanding of the mechanical properties. The plasticity index (H/E ratio or elastic strain to failure) was developed and used to describe the material failure mechanism. At the same time, the wear resistance of a thin film can be calculated from hardness and Young modulus

ratio (H^3/E^2) and gives information on the resistance of the material to plastic deformation [52, 53]. The elastic recovery (ER) of the film was determined using Eq. (5) [46], and the plasticity, which is the ratio of the plastic displacement over the total displacement in the load–displacement curve, was evaluated using Eq. (6) [54]

$$\begin{aligned} \text{Elastic recovery (\%)} &= \frac{h_{\max} - h_{\text{res}}}{h_{\max}} \times 100 \\ &= \frac{\text{elastic deformation}}{\text{total deformation}} \times 100 \end{aligned} \quad (5)$$

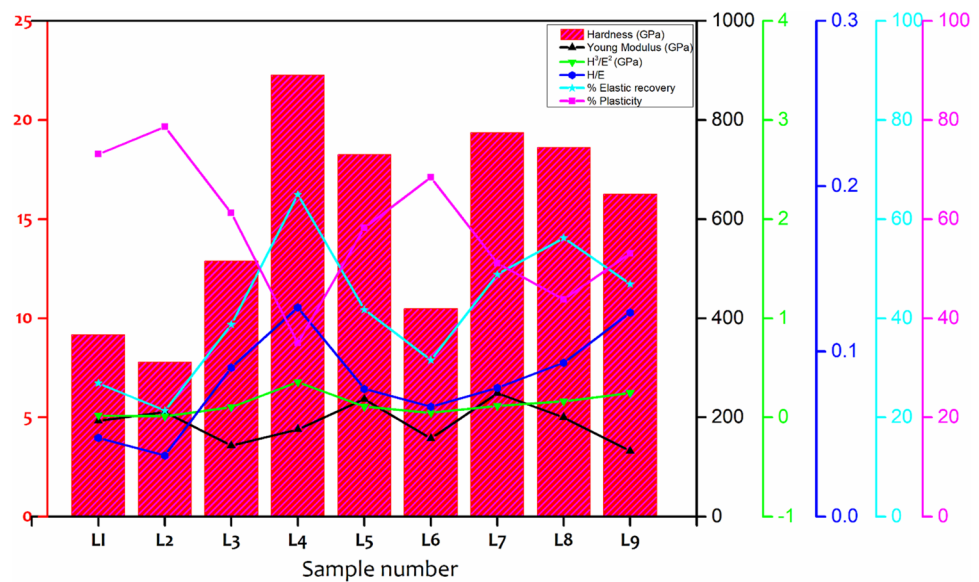
$$\text{Plasticity (\%)} = \frac{h_{\text{res}}}{h_{\max}} \times 100 = \frac{\text{plastic deformation}}{\text{total deformation}} \times 100 \quad (6)$$

From the analysis of the mechanical properties of the coating, it is noticeable that the microstructure and mechanical properties of the coating rely on the interaction of the process parameters used. The interaction between these mechanical responses is illustrated in Fig. 6. From the graph, it can be concluded that a raise in nanohardness produces a raise in H/E, H^3/E^2 and elasticity recovery. Meanwhile, the thin film coating plasticity reduces with an increase in hardness. Furthermore, it has been established that a high H/E ratio suggests an excellent resistance to tribological failure [55, 56]. A decrease in the plasticity and increase in the elastic recovery of the coating indicates an improvement in the coatings' resistance to both elastic and plastic deformation.

4 Conclusion

The research investigated the effect of sputtering on the performance effectiveness of TiC thin film coated on grade 5 (Ti6Al4V) titanium alloys using RF magnetron sputtering under different deposition process parameters. In conclusion, the following findings were observed;

Fig. 6 Graphical representation of the measured and calculated mechanical properties of Ti6Al4V coated with TiC thin film at different powers



- For the physical structure, the FESEM morphology revealed three different growth patterns which depend on the process parameters. Analysis of the roughness of the samples at the nanoscale level performed by AFM agreed with the FESEM results. The topography of the coating shows different growth directions.
- In the case of crystallinity, the (200) preferential orientation plane was visible in the GIXRD analysis and thereby contributed to an effective coating as d-spacing values are above the prescribed for TiC according to the ASTM standard.
- Raman spectra confirm the presence of both D and G band modes. D-band was not visible in L4.
- The hardness improves with an increase in the process parameters. The mechanical strength of sample L4 which is a function of physical and chemical structures outperforms other process parameters considered in this research.

Declarations

Conflict of interest There is no conflict of interest whatsoever.

References

- Eylon D, Vassel A, Combres Y, Boyer R, Bania P, Schutz R (1994) Issues in the development of beta titanium alloys. *JOM J Miner Met Mater Soc* 46:14–15
- Schutz R, Eylon D, Boyer R, Koss D (1993) Beta titanium alloys in the 1990s. The Mineral, Metals & Materials Society, Warrendale, pp 75–91
- Chen Q, Thouas GA (2015) Metallic implant biomaterials. *Mater Sci Eng* 87:1–57
- Donachie MJ (2000) Titanium: a technical guide. ASM International, Russell
- Elias C, Lima J, Valiev R, Meyers M (2008) Biomedical applications of titanium and its alloys. *JOM* 60:46–49
- Williams DF (2008) On the mechanisms of biocompatibility. *Biomaterials* 29:2941–2953
- Williams DF (2009) On the nature of biomaterials. *Biomaterials* 30:5897–5909
- Chen SH, Ho SC, Chang CH, Chen CC, Say WC (2016) Influence of roughness on in-vivo properties of titanium implant surface and their electrochemical behavior. *Surf Coat Technol* 302:215–226
- Boyer R (1996) An overview on the use of titanium in the aerospace industry. *Mater Sci Eng* 213:103–114
- Williams JC, Starke EA Jr (2003) Progress in structural materials for aerospace systems I. *Acta Mater* 51:5775–5799
- Walczak M, Gaska D, Sidor J (2009) Properties and application titanium and titanium alloys in aerospace systems. *Mod Tech Mech Eng* 2009:125
- Starke EA (2001) Aerospace materials for future technologies. *Jpn Inst Light Met J* 51:77–85
- Veiga C, Davim J, Loureiro A (2012) Properties and applications of titanium alloys: a brief review. *Rev Adv Mater Sci* 32:133–148
- Gorynin I (1999) Titanium alloys for marine application. *Mater Sci Eng* 263:112–116
- Leyens C, Peters M (2003) Titanium and titanium alloys: fundamentals and applications. Wiley, Hoboken
- Domínguez-Trujillo C, Ternero F, Rodríguez-Ortiz J, Heise S, Boccaccini A, Lebrato J, Torres Y (2018) Bioactive coatings on porous titanium for biomedical applications. *Surf Coat Technol* 349:584–592
- L. T. Kuhn (2012) Chapter 5—Biomaterials. Pp. 219–271.
- Li Y, Yang C, Zhao H, Qu S, Li X, Li Y (2014) New developments of Ti-based alloys for biomedical applications. *Materials* 7:1709–1800

19. Longo G, Girasole M, Pompeo G, Cricenti A, Misiano C, Acclavio A, Tizzoni AC, Mazzola L, Santini P, Politi L (2010) Effect of titanium carbide coating by ion plating plasma-assisted deposition on osteoblast response: a chemical, morphological and gene expression investigation. *Surf Coat Technol* 204:2605–2612
20. Carbide N (1997) *Boride materials-synthesis and processing*, edited by Aw Weimer. Chapman & Hall, London
21. Upadhyay P, Reynolds A (2012) Effects of forge axis force and backing plate thermal diffusivity on Fsw of Aa6056. *Mater Sci Eng* 558:394–402
22. Wang B, Liu Y, Liu Y, Ye J (2012) Mechanical properties and electronic structure Of Tic, Ti0. 75w0. 25c, Ti0. 75w0. 25c0. 75n0. 25, Tic0. 75n0. 25 and Tin. *Phys B* 407:2542–2548
23. Häglund J, Grimvall G, Jarlborg T, Guillermet AF (1991) Band structure and cohesive properties of 3d-transition-metal carbides and nitrides with the NaCl-type structure. *Phys Rev B* 43:14400
24. Abegunde OO, Akinlabi ET, Oladijo OP, Akinlabi S, Ude AU (2019) Overview of thin film deposition techniques. *Aims Mater Sci* 6:174
25. Scherrer P (1918) Nachrichten von der gesellschaft der wissenschaften zu göttingen. *Math Phys Klasse* 2:98–100
26. Oliver WC, Pharr GM (1992) An improved technique for determining hardness and elastic modulus using load and displacement sensing indentation experiments. *J Mater Res* 7:1564–1583
27. Oliver WC, Pharr GM (2004) Measurement of hardness and elastic modulus by instrumented indentation: advances in understanding and refinements to methodology. *J Mater Res* 19:3–20
28. Bec S, Tonck A, Georges J, Georges E, Loubet J (1996) Improvements in the indentation method with a surface force apparatus. *Philos Mag A* 74:1061–1072
29. Abegunde OO, Esther A, Oladijo OP, Majumdar JD (2019) Surface Integrity of tic thin film produced by Rf magnetron sputtering. *Proc Manuf* 35:950–955
30. Karabacak T (2011) Thin-film growth dynamics with shadowing and re-emission effects. *J Nanophoton* 5:052501
31. Braic M, Zoita N, Danila M, Grigorescu C, Logofatu C (2015) Hetero-epitaxial growth of TiC films on Mgo (001) at 100°C by DC reactive magnetron sputtering. *Thin Solid Films* 589:590–596
32. Mattox DM (1998) Atomistic film growth and some growth-related film properties-9. Elsevier, Amsterdam
33. Chawla V, Jayaganthan R, Chawla A, Chandra R (2009) Microstructural characterisations of magnetron sputtered Ti films on glass substrate. *J Mater Process Technol* 209:3444–3451
34. Ghorannevis Z, Akbarnejad E, Elahi AS, Ghoranneviss M (2016) Application of Rf magnetron sputtering for growth of Azo on glass substrate. *J Cryst Growth* 447:62–66
35. Duan J, Liu J, Mo D, Yao H, Maaz K, Chen Y, Sun Y, Hou M, Qu X, Zhang L (2010) Controlled crystallinity and crystallographic orientation of Cu nanowires fabricated in ion-track templates. *Nanotechnology* 21:365605
36. Duan J, Liu J, Yao H, Mo D, Hou M, Sun Y, Chen Y, Zhang L (2008) Controlled synthesis and diameter-dependent optical properties of Cu nanowire arrays. *Mater Sci Eng* 147:57–62
37. Wang H, Zhang S, Li Y, Sun D (2008) Bias effect on microstructure and mechanical properties of magnetron sputtered nanocrystalline titanium carbide thin films. *Thin Solid Films* 516:5419–5423
38. Oláh N, Fogarassy Z, Sulyok A, Sáfrán E, Furkó M, Csanádi T, Balázs K (2016) Structural investigation, corrosion properties and adhesion behavior of magnetron-sputtered nanocomposite Tic/A: C thin film coatings. *European microscopy congress 2016: proceedings*. Wiley, Hoboken, pp 1014–1015
39. Ferrari AC, Robertson J (2000) Interpretation of Raman spectra of disordered and amorphous carbon. *Phys Rev B* 61:14095
40. Deng X, Huang J, Sun Y, Liu K, Gao R (2016) Effect of processing parameters on the structural, electrical and magnetic properties of Bfo thin Fi Lm synthesised via Rf magnetron sputtering. *J Alloys Compd* 684:510–515
41. Terrones H, Del Corro E, Feng S, Poumirol J, Rhodes D, Smirnov D, Pradhan N, Lin Z, Nguyen M, Elias A (2014) New first order raman-active modes in few layered transition metal dichalcogenides. *Sci Rep* 4:4215
42. Ma T, Wang L, Hu Y, Li X, Wang H (2014) A shear localisation mechanism for lubricity of amorphous carbon materials. *Sci Rep* 4:3662
43. Hong J, Park MK, Lee EJ, Lee D, Hwang DS, Ryu S (2013) Origin of new broad Raman D and G Peaks in annealed graphene. *Sci Rep* 3:2700
44. Klein M, Holy JA, Williams W (1978) Raman scattering induced by carbon vacancies in Ti C X. *Phys Rev B* 17:1546
45. Zeng XT (1999) Tin/Nbn superlattice hard coatings deposited by unbalanced magnetron sputtering. *Surf Coat Technol* 113:75–79
46. Kumar DD, Kumar N, Kalaiselvam S, Dash S, Jayavel R (2017) Wear resistant super-hard multilayer transition metal-nitride coatings. *Surf Interfaces* 7:74–82
47. Gilley KL, Nino JC, Riddle YW, Hahn DW, Perry SS (2012) Heat treatments modify the tribological properties of nickel boron coatings. *ACS Appl Mater Interfaces* 4:3069–3076
48. Friedman LH, Chrzan D (1998) Scaling theory of the hall-petch relation for multilayers. *Phys Rev Lett* 81:2715
49. Kumar DD, Kumar N, Kalaiselvam S, Radhika R, Maximus Rabel A, Jayavel R (2017) Tribo-mechanical properties of reactive magnetron sputtered transition metal carbide coatings. *Tribol Int* 114:234–244
50. Caicedo JC, Amaya C, Yate L, Gómez ME, Zambrano G, Alvarado-Rivera J, Muñoz-Saldaña J, Prieto P (2010) Ticn/Tinbcn multilayer coatings with enhanced mechanical properties. *Appl Surf Sci* 256:5898–5904
51. Mockute A, Palisaitis J, Alling B, Berastegui P, Broitman E, Näslund L, Nedfors N, Lu J, Jensen J, Hultman L (2017) Age hardening in (Ti1–Xalx) B2 Δ thin films. *Scr Mater* 127:122–126
52. Musil J, Novák P, Čerstvý R, Soukup Z (2010) Tribological and mechanical properties of nanocrystalline-Tic/A-C nanocomposite thin films. *J Vac Sci Technol A* 28:244–249
53. Oláh N, Fogarassy Z, Sulyok A, Szívós J, Csanádi T, Balázs K (2016) Ceramic Tic/A: C protective nanocomposite coatings: structure and composition versus mechanical properties and tribology. *Ceram Int* 42:12215–12220
54. Zhang S, Sun D, Fu Y, Du H (2005) Toughness measurement of thin films: a critical review. *Surf Coat Technol* 198:74–84
55. Leyland A, Matthews A (2000) On the significance of the H/E ratio in wear control: a nanocomposite coating approach to optimised tribological behaviour. *Wear* 246:1–11
56. Abegunde OO, Akinlabi ET, Oladijo OP (2020) Influence of sputtering parameters on the structural and mechanical properties of Tic thin film coating. *Appl Surface Sci* 520:146323

Publisher's Note Springer Nature remains neutral with regard to jurisdictional claims in published maps and institutional affiliations.